Journal of Advanced Ceramics
2020, **9**(1): 35–44
https://doi.org/10.1007/s40145-019-0345-1
ISSN 2226-4108
CN 10-1154/TQ

Research Article

Molten salt synthesis, formation mechanism, and oxidation behavior of nanocrystalline HfB_2 powders

Da LIU[a], Qiangang FU[b], Yanhui CHU[a,*]

[a]*School of Materials Science and Engineering*, *South China University of Technology*, *Guangzhou 510641*, *China*
[b]*State Key Laboratory of Solidification Processing*, *Northwestern Polytechnical University*, *Xi'an 710072*, *China*

Received: April 1, 2019; Revised: June 19, 2019; Accepted: July 20, 2019

Abstract: Nanocrystalline HfB_2 powders were successfully synthesized by molten salt synthesis technique at 1373 K using B and HfO_2 as precursors within KCl/NaCl molten salts. The results showed that the as-synthesized powders exhibited an irregular polyhedral morphology with the average particle size of 155 nm and possessed a single-crystalline structure. From a fundamental aspect, we demonstrated the molten-salt assisted formation mechanism that the molten salts could accelerate the diffusion rate of the reactants and improve the chemical reaction rate of the reactants in the system to induce the synthesis of the high-purity nanocrystalline powders. Thermogravimetric analysis showed that the oxidation of the as-synthesized HfB_2 powders at 773–1073 K in air was the weight gain process and the corresponding oxidation behavior followed parabolic kinetics governed by the diffusion of oxygen in the oxide layer.

Keywords: ultra-high temperature ceramics; powders; molten salt synthesis; oxidation behavior

1 Introduction

As members of ultra-high temperature ceramics, transition-metal borides (TMB_2) ceramics have attracted considerable attentions for potential applications in aircraft, atomic, and astronautic manufacturing industries, since they exhibit high melting point, high hardness, high thermal conductivity, and excellent chemical stability [1–3]. The synthesis of TMB_2 powders is critical for implementing their extensive applications. Up to now, a variety of techniques have been developed to synthesize TMB_2 powders, such as mechanochemically assisted method [4–7], carbo/borothermal reduction [8–10], sol–gel method [11–13], and so on. However, the reported techniques for synthesizing TMB_2 powders have some shortcomings, such as the high synthesis temperatures and expensive reaction precursors. In addition, the as-obtained powders possess the large particle size. Therefore, a low temperature technique for synthesizing TMB_2 ultrafine powders is of vital importance for implementing the extensive applications of TMB_2 ceramics. Recently, a low temperature molten salt synthesis technique has been proposed to synthesize TMB_2 ultrafine powders including NbB_2 [14], TiB_2 [15], and CrB_2 [16]. Nevertheless, the current understanding of the molten-salt assisted formation mechanism is yet limited, and the synthesis of much more TMB_2 ultrafine powders by the molten salt synthesis technique has rarely been reported until now. In addition, there is seldom report so far on the oxidation behavior of TMB_2 nanopowders, which is a critical property for high-temperature applications.

* Corresponding author.
E-mail: chuyh@scut.edu.cn

HfB_2 ceramics, as a member of TMB_2 ceramics, have recently attracted extensive attentions because they exhibit potential applications in high-temperature electrodes and thermal protection systems for hypersonic aerospace vehicles [17–20]. In this work, we successfully synthesized the nanocrystalline HfB_2 powders by the molten salt synthesis technique at a relatively low temperature of 1373 K using the inexpensive HfO_2 and B powders as reaction precursors within the inexpensive KCl/NaCl molten salts. The effect of synthesis temperatures and molten salts on the phase compositions, morphology, and microstructure of the as-synthesized powders was investigated in detail, as well as the molten-salt assisted formation mechanism. The oxidation behavior of the as-synthesized powders was also investigated at different temperatures.

2 Experimental

The synthesis of HfB_2 powders was conducted by the molten-salt assisted borothermal reduction based on the reaction between HfO_2 powders (99.9% purity, average particle size: 1–3 μm, Shanghai Chaowei Nanotechnology Co., Ltd., Shanghai, China) and amorphous B powders (purity: 99.9%, average particle size < 3 μm, Shanghai Chaowei Nanotechnology Co., Ltd., Shanghai, China) with the presence of NaCl/KCl molten salts (molar ratio: 1:1, eutectic point: 931 K). The molar ratio was 3:10 for HfO_2/B and 1:1 for NaCl/KCl, respectively. The weight ratio was 10:1 for NaCl/KCl and HfO_2/B. Details of the synthesis of HfB_2 powders were described as follows: The starting materials of HfO_2, B, and NaCl/KCl were first mixed by hand for 30 min in an agate mortal using an agate pastel, and then the mixture of raw materials was put into an alumina crucible and placed into the horizontal alumina tube furnace. After evacuating the furnace for three times, argon carrier gas (purity: 99.99%) was introduced into the system with a flow rate of 300 sccm (standard-state cubic centimeter per minute). The system was heated from room temperature to 1273–1373 K at a rate of 10 K/min and held for 1 h, followed by furnace cooling to room temperature. Afterwards the as-synthesized products were taken out and immersed in the deionized water at 353 K to dissolve the residual NaCl/KCl salts, and B_2O_3 production. Finally, they were filtered and washed by the deionized water and the absolute ethanol for several times, and dried at 333 K. The products were also prepared by the similar borothermal reduction method without NaCl/KCl molten salts for comparison.

Thermogravimetric analysis (TGA) of the as-synthesized powders was performed using a Metter Toledo Star TGA/SDTA 851 thermal analyzer to investigate their isothermal oxidation behaviors at different temperatures. Before the isothermal oxidation tests, the surface area of the as-synthesized HfB_2 powders was first measured to be about 3.5 $m^2 \cdot g^{-1}$ by Brunauer–emmett–teller Test method. Afterwards the samples were heated to the desired temperatures (773, 873, 973, and 1073 K) for the isothermal oxidation tests in air. The fast heating stage with a heating rate of 50 K/min prior to the isothermal period was applied to minimize oxidation effects before reaching the target temperatures in flowing nitrogen (purity: 99.99%) with a flow rate of 50 sccm. Finally, they were cooled naturally to room temperature in flowing nitrogen with a flow rate of 50 sccm. Weight changes of the as-synthesized powders related to the oxidation time were recorded with thermogravimetric mode.

The samples were analyzed by X-ray diffraction (XRD, X'pert PRO; PANalytical, Almelo, the Netherlands), scanning electron microscopy (SEM, Supra-55; Zeiss, Oberkochen, Germany), and transmission electron microscopy (TEM, Tecnai F30G2; FEI, Eindhoven, the Netherlands) equipped with energy dispersive spectroscopy (EDS).

3 Results and discussion

XRD patterns of the as-synthesized products at various conditions are shown in Fig. 1. Clearly, after incorporating molten salts, it can be seen that the products synthesized at 1273 K consist of a dominant HfB_2 phase and a minor HfO_2 impurity phase, as displayed in Fig. 1(a). However, when the synthesis temperature rises to 1373 K, the diffraction peaks of HfO_2 impurity phase disappear and only the diffraction peaks of HfB_2 phase can be detected in the as-synthesized products, as shown in Fig. 1(b). This indicates that HfB_2 products can be successfully synthesized at 1373 K with molten salts. Before incorporating molten salts, the products synthesized at 1373 K are composed of HfB_2 phase and HfO_2 impurity phase, as presented in Fig. 1(c). Obviously, a high content of HfO_2 impurity phase is present in the as-synthesized products. This suggests that HfB_2 products cannot be synthesized at 1373 K

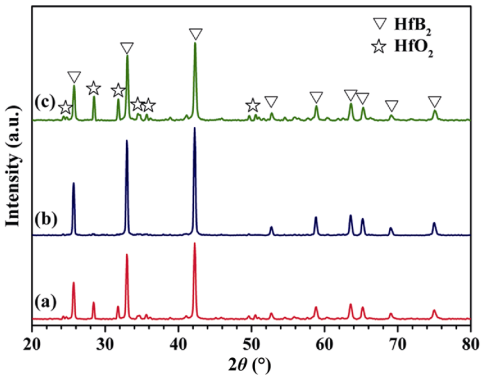

Fig. 1 XRD patterns of the as-synthesized products at different conditions: (a) 1273 K with molten salts, (b) 1373 K with molten salts, and (c) 1373 K without molten salts.

without molten salts, which clearly demonstrates that the presence of molten salts induces the synthesis of HfB_2 products.

SEM images of HfB_2 products synthesized at 1373 K with molten salts are displayed in Fig. 2. From Fig. 2(a), it is evident that the as-synthesized products consist of a large amount of small particles. The high magnification SEM image shows that these small particles possess an irregular polyhedral morphology with the relatively uniform particle sizes, as shown in Fig. 2(b). In addition, SEM image can be examined to determine their particle sizes. A total of 100 individual particles were measured to get the average value of particle sizes and a Gaussian fitting to these data yields an average particle size of 155 nm (Fig. 2(c)). Therefore, the nanocrystalline HfB_2 powders can be successfully synthesized at 1373 K with molten salts.

Figure 3(a) shows a typical TEM image of HfB_2 powders synthesized at 1373 K with molten salts, from which it can be clearly observed that the as-synthesized powders involve a large number of individual nanocrystalline particles. Clearly, their particle sizes can also be determined based on TEM images. A total of 50 individual particles were measured to get the average value of particle sizes. A Gaussian fitting to these data yields an average particle size of 155 nm, as shown in the inserted histogram in Fig. 3(a), which is in good agreement with the measured results from SEM images (Fig. 2(c)). Figure 3(b) shows a representative selected area electron diffraction (SAED) pattern along zone axis [111] of the as-synthesized powders. It clearly exhibits that the as-synthesized powders are the single crystal and hexagonal structure of HfB_2 due to the well-arranged diffraction spots with the symmetry. The high-resolution transmission electron microscopy (HRTEM) image of the as-synthesized powders in Fig. 3(c) shows a periodic lattice structure and a set of fringes with the *d*-spaces of 0.272 nm, corresponding to the (110) plane of HfB_2 (JCPSD Card No. 12-0234), which further confirms that the as-synthesized powders are single-crystalline hexagonal HfB_2. In addition, an obvious amorphous B_2O_3 layer of ~4 nm can be seen on each particle surface (marked by dotted red lines in Fig. 3(c)), which could account for the presence of O element in EDS spectrum, as displayed in Fig. 4(d). The scanning transmission electron microscopy (STEM)–EDS analysis was further performed at an acceleration voltage of 200 kV and a collection time of 230 s. Besides O element, EDS spectrum also reveals that the as-synthesized powders contain Hf, B, and Cu elements. The presence of Hf and B elements verifies that the as-synthesized powders are composed of HfB_2 phases. The detected Cu element should be attributed to the copper grids used to support TEM samples.

On the basis of the aforementioned experiment

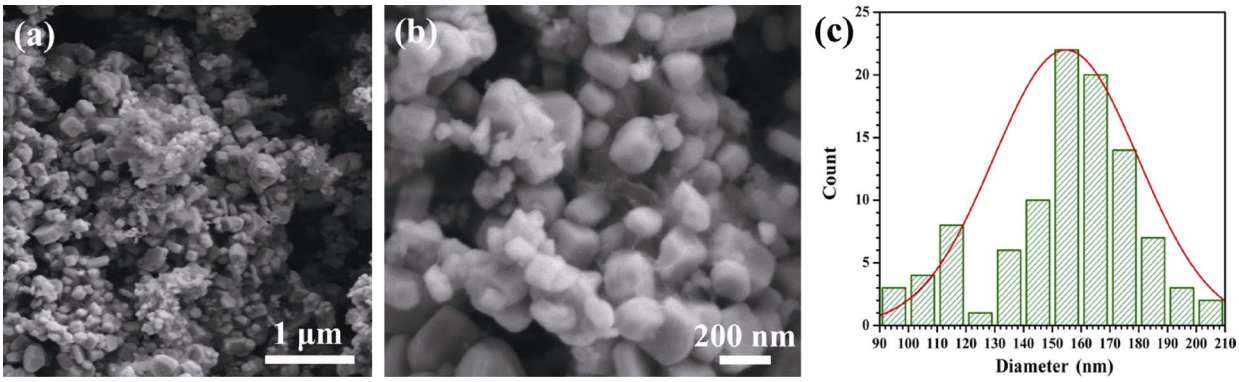

Fig. 2 SEM characterizations of HfB_2 products synthesized at 1373 K with molten salts: (a) low magnification SEM image and (b) high magnification SEM image. (c) Histogram of each measured data for the particle sizes with a Gaussian fitting to the data. The Gaussian peak is centered at 155 nm.

results, it can be concluded that the presence of molten salts is crucial for the synthesis of the nanocrystalline HfB_2 powders in our work. Similar conclusions have also been reported previously in other TMB_2 ultrafine powders synthesized by the molten-salt assisted method, such as NbB_2 [14], TiB_2 [15], and CrB_2 [16]. However, the molten-salt assisted formation mechanism is not well understood. To better understand this mechanism, we establish two simple schematic diagrams of formation mechanisms associated to the as-synthesized HfB_2 powders without molten salts and with molten salts, as shown in Fig. 4.

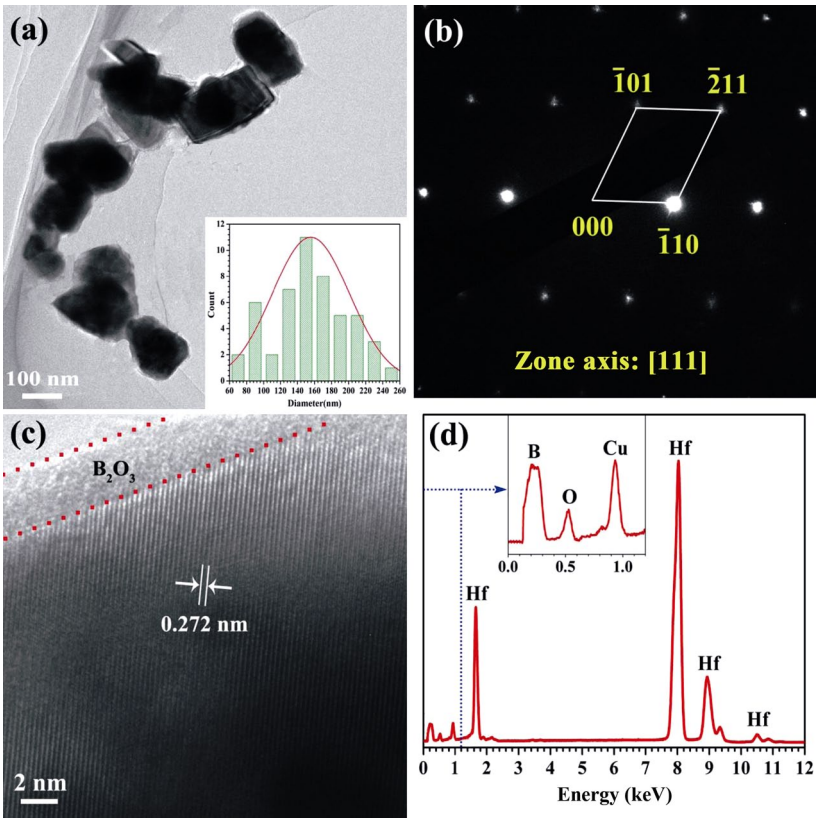

Fig. 3 TEM analysis of HfB_2 products synthesized at 1373 K with molten salts: (a) TEM image, (b) SAED pattern, (c) HRTEM image, and (d) EDS spectrum.

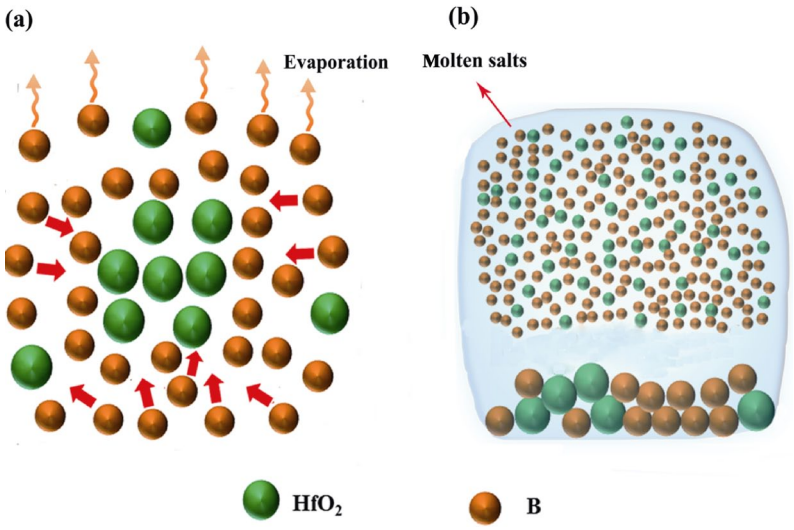

Fig. 4 Schematic diagrams of formation mechanisms associated to the as-synthesized HfB_2 powders: (a) without molten salts and (b) with molten salts.

In our case, the reaction precursors of the system involve HfO_2 powders and amorphous B powders. NaCl/KCl is only used as molten salts. As a result, before incorporating molten salts, the synthesis of HfB_2 powders is a traditional solid–solid reaction process, in which B reactant will first diffuse to the surface of HfO_2 reactant and then it reacts with HfO_2 to generate HfB_2 product at synthesis temperatures, as displayed in Fig. 4(a). The reaction as well as the correlation between the standard Gibbs free energy ($\Delta G^{\theta}_{R,T}$) of this reaction and the oxidation temperature (T) can be described as follows [21]:

$$\begin{gathered} 3HfO_2+10B \rightarrow 3HfB_2+2B_2O_3 \\ \Delta G^{\theta}_{R,T} = -236,634 - 3T \end{gathered} \tag{1}$$

where R is the gas constant. It is evident that the standard Gibbs free energy of Reaction (1) is so negative that this reaction can occur spontaneously at synthesis temperatures. After incorporating molten salts, the synthesis of HfB_2 powders is a new molten-salt assisted liquid–solid reaction process, as presented in Fig. 4(b). In this process, the molten salts will be first melted into isotropic liquid at elevated temperatures, and then the B and HfO_2 reactants are rapidly dissolved into the molten salts. This finally leads to the uniformly distributions of B and HfO_2 in the molten salts. Afterwards HfB_2 product is generated by Reaction (1) between the B and HfO_2 reactants at synthesis temperatures by Eq. (1). With the reaction continuing, the dissolved reactants are constantly consumed, but at the same time the undissolved reactants are continuously dissolved into molten salts to participate in the reaction until the end. In general, the total reaction rate (V) of the system depends on the diffusion rate (V_D) of the reactants and the chemical reaction rate (V_R) of the reactants, which can be calculated by the following equations [22]:

$$V = \frac{1}{\frac{1}{V_D} + \frac{1}{V_R}} \tag{2}$$

$$V_D = D_0 \times \exp\left(-\frac{Q}{RT}\right)\left(\frac{C_0 - C}{\delta}\right) \tag{3}$$

$$V_R = KC^3_{HfO_2}C^{10}_B \tag{4}$$

where Q is the diffusion activation energy, D_0 is the constant of coefficient of diffusion, C_0 is the reactant concentration at the beginning of diffusion, C is the reactant concentration at the end of diffusion, δ is the diffusion distance, K is the chemical reaction constant, C_{HfO_2} and C_B are the HfO_2 and B concentrations, respectively. From Eq. (3), it can be found that the diffusion rate of the reactants is closely related to the diffusion distance and the diffusion activation energy. Before incorporating molten salts, there is a long diffusion distance in the reactants due to their agglomerations, as shown in Fig. 4(a). After incorporating molten salts, the B and HfO_2 reactants are uniformly dispersed into the molten salts, and thereby a short diffusion distance is presented in the reactants, as displayed in Fig. 4(b). In addition, as a rule, the diffusion activation energy of the reactants in the liquid phase is much less than that in the solid phase. As a consequence, both the short diffusion distance and the reduced diffusion activation energy result in the presence of a large diffusion rate in the molten-salt assisted synthesis process. From Eq. (4), we can see that the chemical reaction rate of the reactants is mainly determined by the HfO_2 and B concentrations. In general, B reactant is very easy to be volatilized at elevated temperatures. However, the degree of B evaporation in liquid phase is less than that in solid phase. Consequently, B reactant possesses a high concentration in the molten-salt assisted synthesis process, which could significantly enhance the chemical reaction rate of the reactants. In brief, the presence of molten salts not only accelerates the diffusion rate of the reactants by shortening their diffusion distances and decreasing their diffusion activation energies, but also enhances the chemical reaction rate by reducing the evaporation of B. Owing to the high diffusion rate and chemical reaction rate, according to Eq. (2), it can be clearly observed that the total reaction rate of the system will be high in the molten-salt assisted synthesis process, which finally results in the synthesis of the nanocrystalline HfB_2 powders.

To investigate the isothermal oxidation behavior of the as-synthesized HfB_2 powders at different temperatures, the TGA test was conducted and the results are shown in Fig. 5.

From Fig. 5(a), it can be seen that the oxidation of the samples at 773 and 873 K exhibits the weight gain process. However, the oxidation rate of the samples at 873 K is much higher than that of the samples at 773 K. After isothermal oxidation for 120 min in air, the weight gain of the samples at 773 K is only 0.034 mg/cm^2, while the weight gain of the samples at 873 K is up to 0.116 mg/cm^2. Figure 5(b) depicts the plots of the square of the specific weight change as a function of

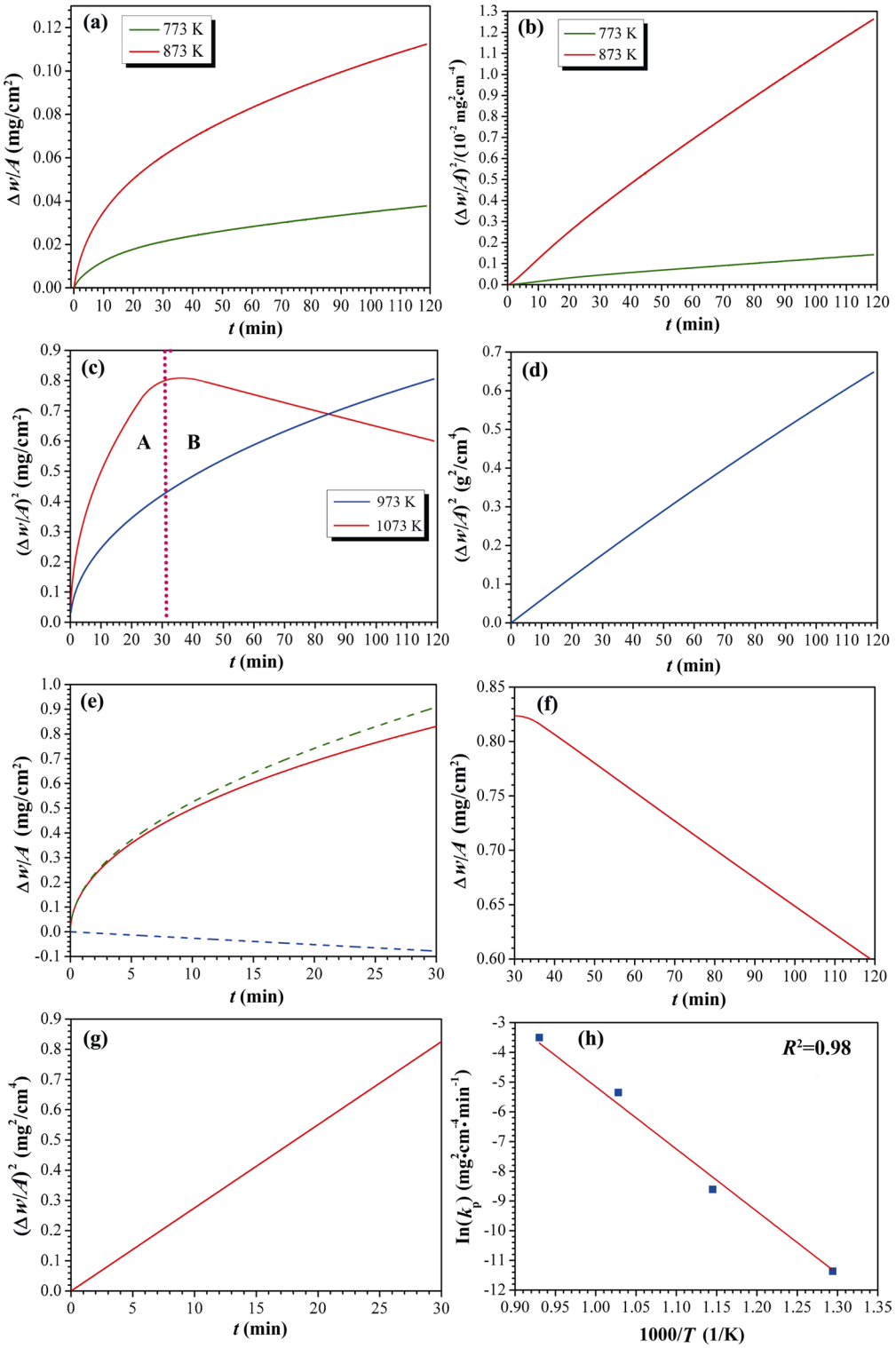

Fig. 5 Oxidation analysis of the as-synthesized HfB_2 powders by TGA tests at different temperatures: (a) weight change per unit area ($\Delta w/A$, Δw is the weight change and A is the surface area of samples) as a function of oxidation time (t) at 773 and 873 K; (b) square of the weight change per unit surface area as a function of oxidation time at 773 and 873 K; (c) weight change per unit area as a function of oxidation time at 973 and 1073 K; (d) square of the weight change per unit surface area as a function of oxidation time at 973 K; (e) weight change per unit area as a function of oxidation time at 1073 K after 30 min; (f) weight change per unit area as a function of oxidation time at 1073 K before 30 min with fitted parabolic and line curves; (g) square of the weight change per unit surface area corresponding to the fitted parabolic curve in (f); (h) plot of logarithm parabolic rate k_p (parabolic rate constant) versus reciprocal of the temperatures.

oxidation time for the samples at 773 and 873 K. Clearly, there is a good linear relationship ($R^2 > 0.99$) between the square of the specific weight change and oxidation time, which indicates that the oxidation behavior of the samples at 773 and 873 K follows the parabolic kinetics. That is to say, the oxidation of the samples at 773 and 873 K is governed by a diffusion process that oxygen diffused into the oxide layer generated in the reaction between HfB_2 and O_2 by the following equation [23,24]:

$$2HfB_2+5O_2 \rightarrow 2HfO_2+2B_2O_3 \quad (5)$$

As the oxidation temperature rises to 973 K, the oxidation of the samples is still a weight gain process and their oxidation behavior also follows a parabolic kinetics (Figs. 5(c) and 5(d)). However, the weight gain of the samples is up to 0.8 mg/cm^2 after isothermal oxidation for 120 min in air, much larger than that of the samples at 873 K, suggesting that the oxidation rate of the samples at 973 K is quite high. When the oxidation temperature increases to 1073 K, the oxidation of the samples is a complicated weight gain process, as displayed in Fig. 5(c), which can be divided into two stages, marked as A and B, respectively. During the stage A (0–30 min), the oxidation of the samples exhibits a rapid weight gain and the final weight gain is up to 0.82 mg/cm^2 after isothermal oxidation for 30 min in air. As the oxidation time is over 30 min (stage B), the oxidation of the samples is still a weight gain process, but the weight gain rate is negative. Hence, the final weight gain decreases to 0.6 mg/cm^2 after isothermal oxidation for 120 min in air. In addition, From Eq. (5), it can be found that the oxidation of the samples is a weight gain process. Therefore, it can be concluded that the samples have been completely oxidized after isothermal oxidation for 30 min at 1073 K in air. After isothermal oxidation for 30 min, the weight gain of the samples is a linear decrease process (Fig. 5(f)), which should be associated to the evaporation of B_2O_3. On the basis of this linear relationship, a constant evaporation rate of B_2O_3 can be calculated to be ~0.026 mg/(cm^2·min^{-1}). Before isothermal oxidation for 30 min, it should be noted that the oxidation behavior of the samples deviates from the parabolic kinetics, as shown in Fig. 5(e). Therefore, a simple parabolic law is unable to describe the oxidation kinetic behavior. However, the TGA curve can be fitted into a linear term and a parabolic term based on a multiple-law model, according to the following equation [25]:

$$\frac{\Delta w}{A} = k_1 t + k_p \sqrt{t} \quad (6)$$

where k_1 is the linear rate constant. The results are depicted in Fig. 5(e). Obviously, the dominating term is still a parabolic curve (green dotted line), which suggests that the oxidation behavior of the samples is still a parabolic kinetics before isothermal oxidation for 30 min at 1073 K in air. This can be further confirmed by the presence of a good linear relationship between the square of the specific weight change and oxidation time, as depicted in Fig. 5(g). The rest term is a linear curve (blue dotted line) and it is negative, which is associated with the evaporation of B_2O_3. This is because that the slop of the line can be calculated to be ~0.025 mg/(cm^2·min^{-1}), which is consistent with the vaporization rate of B_2O_3 (0.026 mg/(cm^2·min^{-1})) after isothermal oxidation for 30 min. In sum, the oxidation behavior of the samples follows the parabolic kinetics at 773–1073 K, which is governed by the diffusion of oxygen in the oxide layer. As a result, k_p at various oxidation temperatures can be calculated by the following equation [26]:

$$w^2 = k_p t \quad (7)$$

The calculated results are listed in Table 1. On the basis of these results, for the oxygen diffusion mode, the oxidation activation energy (ΔE) of the samples can be also calculated by the following equation [27]:

$$k_p = A_0 \exp\left(\frac{\Delta E}{RT}\right) \quad (8)$$

where A_0 is the constant of preexponential factor. Figure 5(h) plots the In(k_p) as a function of reciprocal temperatures, and thereby the oxidation activation energy can be calculated to be ~190.8 kJ/mol.

Figure 6 shows that XRD patterns of the as-synthesized HfB_2 powders after isothermal oxidation tests at various temperatures. After isothermal oxidation tests at 773 and 873 K, the as-synthesized HfB_2 powders are

Table 1 Calculated k_p with corresponding R^2 (fit goodness) for various oxidation temperatures

Oxidation temperature (K)	k_p (mg^2·cm^{-4}·min^{-1})	R^2
773	0.0000116	0.999
873	0.000105	0.997
973	0.0054	0.994
1073	0.0253	—

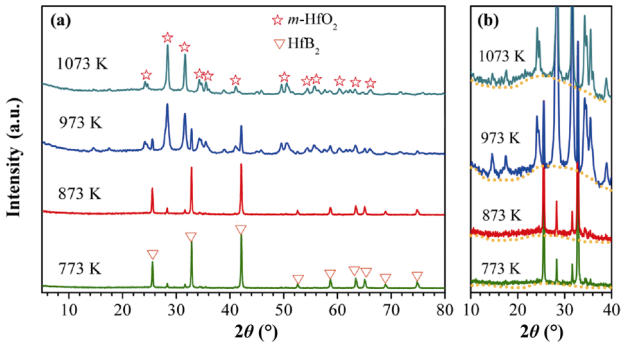

Fig. 6 XRD analysis of the as-synthesized HfB_2 powders after oxidation tests: (a) XRD patterns of the as-synthesized HfB_2 powders after oxidation tests at various temperatures; (b) high magnification of XRD patterns with 2θ from 10° to 40°.

mainly composed of a dominant HfB_2 phase and a minor HfO_2 phase, as displayed in Fig. 6(a), which suggests that only a small number of HfB_2 powders are oxidized at 773 and 873 K. As the oxidation temperature rises to 973 K, the as-synthesized HfB_2 powders mainly consist of a dominant HfO_2 phase and a minor HfB_2 phase, indicating that most of HfB_2 powders have been oxidized at 973 K. When the oxidation temperature increases to 1073 K, the diffraction peaks of HfB_2 phase have completely disappeared in the XRD pattern and all the relatively sharp diffraction peaks in the XRD pattern can be indexed to HfO_2 phase. These imply that HfB_2 powders have been completely oxidized at 1073 K. What's more, the amorphous B_2O_3 can also be detected by XRD, as depicted in Fig. 6(b). A weak diffraction peak near a 2θ value of 28° from the {310} lattice plane of the amorphous B_2O_3 product can be observed at 773 and 873 K, while its intensity becomes very remarkable when the oxidation temperatures rise to 973 and 1073 K. This further confirms that only a small number of HfB_2 powders are oxidized at 773 and 873 K, while most or all of HfB_2 powders have been oxidized at 973 and 1073 K.

Figure 7 shows that the SEM images of the as-synthesized HfB_2 powders after isothermal oxidation tests at various temperatures. After isothermal oxidation tests at 773 and 873 K, the powders mainly consist of the irregularly HfB_2 particles, on which some amorphous B_2O_3 glass and HfO_2 nanoparticles can be found, as shown in Figs. 7(a) and 7(b). This suggests that the powders are only oxidized slightly at 773 and 873 K. As the oxidation temperature rises to 973 K, the powders are mainly composed of numerous HfO_2 nanoparticles and amorphous B_2O_3 glass, and only a few irregularly HfB_2 particles can be observed, indicating that most of HfB_2 powders have been oxidized at 973 K. When the oxidation temperature increases to 1073 K, the powders involve numerous HfO_2 nanoparticles, nanorods, and amorphous B_2O_3 glass phase can be found, which

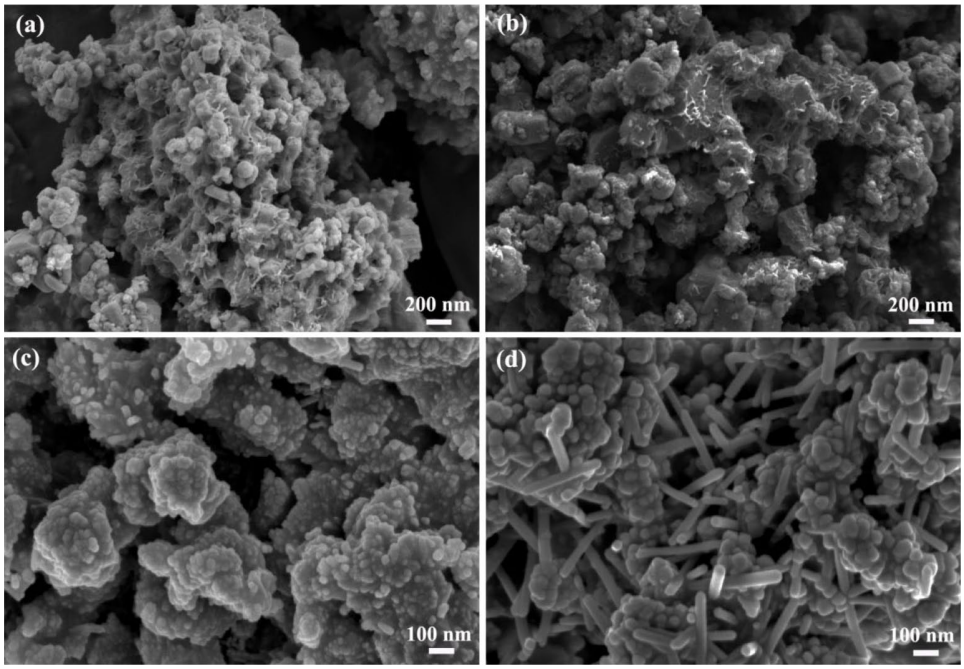

Fig. 7 SEM images of the as-synthesized HfB_2 powders after oxidation tests at various temperatures in air: (a) 773, (b) 873, (c) 973, and (d) 1073 K.

implies that all of HfB_2 powders have been completely oxidized at 973 K.

4 Conclusions

In summary, the nanocrystalline HfB_2 powders had been successfully synthesized via a simple molten salt synthesis technique. The as-synthesized HfB_2 powders possessed an irregular polyhedral morphology with the average particle sizes of ~155 nm. In addition, they also exhibited a single-crystalline structural feature. More importantly, from a fundamental aspect, we demonstrated why the presence of molten salts could induce the synthesis of nanocrystalline HfB_2 powders. The oxidation results show that the oxidation of as-synthesized HfB_2 powders at 773–1073 K in air is the weight gain process and the corresponding oxidation behavior follows parabolic kinetics that is governed by the diffusion of oxygen in the oxide layer. This work not only may provide a new method for the synthesis of HfB_2 powders and a theoretical guidance for the molten salt synthesis method, but also reveal the oxidation behaviors of the nanocrystalline HfB_2 powders at low temperatures in air.

Acknowledgements

We acknowledge financial support from the National Key R&D Program of China (No. 2017YFB0703200), National Natural Science Foundation of China (Nos. 51802100 and 51972116), Young Elite Scientists Sponsorship Program by CAST (No. 2017QNRC001), and the fund of the State Key Laboratory of Solidification Processing in NWPU (No. SKLSP201820).

References

[1] Fahrenholtz WG, Hilmas GE, Talmy IG, *et al*. Refractory diborides of zirconium and hafnium. *J Am Ceram Soc* 2007, **90**: 1347–1364.

[2] Gui KX, Liu FY, Wang G, *et al*. Microstructural evolution and performance of carbon fiber-toughened ZrB_2 ceramics with SiC or $ZrSi_2$ additive. *J Adv Ceram* 2018, **7**: 343–351.

[3] Ren XR, Feng PZ, Guo LT, *et al*. Synthesis of ultra-fine TaB_2 nano powders by liquid phase method. *J Am Ceram Soc* 2017, **100**: 5358–5362.

[4] Guo SQ, Hu CF, Kagawa Y. Mechanochemical processing of nanocrystalline zirconium diboride powder. *J Am Ceram Soc* 2011, **94**: 3643–3647.

[5] Radev DD, Klissurski D. Mechanochemical synthesis and SHS of diborides of titanium and zirconium. *J Mater Synth Process* 2001, **9**: 131–136.

[6] Guo SQ, Ping DH, Kagawa Y. Synthesis of zirconium diboride platelets from mechanically activated $ZrCl_4$ and B powder mixture. *Ceram Int* 2012, **38**: 5195–5200.

[7] Chen LY, Gu YL, Shi L, *et al*. Synthesis and oxidation of nanocrystalline HfB_2. *J Alloys Compd* 2004, **368**: 353–356.

[8] Guo WM, Zhang GJ, You Y, *et al*. TiB_2 powders synthesis by borothermal reduction in TiO_2 under vacuum. *J Am Ceram Soc* 2014, **97**: 1359–1362.

[9] Ni DW, Zhang GJ, Kan YM, *et al*. Synthesis of monodispersed fine hafnium diboride powders using carbo/borothermal reduction of hafnium dioxide. *J Am Ceram Soc* 2008, **91**: 2709–2712.

[10] Ma L, Yu JC, Guo X, *et al*. Effects of HBO_2 on phase and morphology of ZrB_2 powders synthesized by carbothermal reduction. *Ceram Int* 2017, **43**: 12975–12978.

[11] Yang BY, Li JP, Zhao B, *et al*. Synthesis of hexagonal-prism-like ZrB_2 by a sol-gel route. *Powder Technol* 2014, **256**: 522–528.

[12] Rabiezadeh A, Hadian AM, Ataie A. Synthesis and sintering of TiB_2 nanoparticles. *Ceram Int* 2014, **40**: 15775–15782.

[13] Patra N, Nasiri NA, Jayaseelan DD, *et al*. Synthesis, characterization and use of synthesized fine zirconium diboride as an additive for densification of commercial zirconium diboride powder. *Ceram Int* 2016, **42**: 9565–9570.

[14] Ran SL, Sun HF, Wei YN, *et al*. Low-temperature synthesis of nanocrystalline NbB_2 Powders by borothermal reduction in molten salt. *J Am Ceram Soc* 2014, **97**: 3384–3387.

[15] Bao K, Wen Y, Khangkhamano M, *et al*. Low-temperature preparation of titanium diboride fine powder via magnesiothermic reduction in molten salt. *J Am Ceram Soc* 2017, **100**: 2266–2272.

[16] Liu ZT, Wei YN, Meng X, *et al*. Synthesis of CrB_2 powders at 800 ℃ under ambient pressure. *Ceram Int* 2017, **43**: 1628–1631.

[17] Zhang GJ, Ni DW, Zou J, *et al*. Inherent anisotropy in transition metal diborides and microstructure/property tailoring in ultra-high temperature ceramics—A review. *J Eur Ceram Soc* 2018, **38**: 371–389.

[18] Jalaly M, Gotor FJ, Sayagués MJ. Self-propagating mechanosynthesis of HfB_2 nanoparticles by a magnesiothermic reaction. *J Am Ceram Soc* 2018, **101**: 1412–1419.

[19] Ren XR, Shang TQ, Wang WH, *et al*. Dynamic oxidation protective behaviors and mechanisms of HfB_2-20wt%SiC composite coating for carbon materials. *J Eur Ceram Soc* 2019, **39**: 1955–1964.

[20] Liang H, Guan SX, Li X, *et al*. Microstructure evolution, densification behavior and mechanical properties of nano-HfB_2 sintered under high pressure. *Ceram Int* 2019, **45**: 7885–7893.

[21] Fahrenholtz WG, Binner J, Zou J. Synthesis of ultra-refractory transition metal diboride compounds. *J Mater Res* 2016, **31**: 2757–2772.
[22] Toyoura K, Koyama Y, Kuwabara A, *et al*. First-principles approach to chemical diffusion of lithium atoms in a graphite intercalation compound. *Phys Rev B* 2008, **78**: 214303.
[23] Parthasarathy TA, Rapp RA, Opeka M, *et al*. A model for the oxidation of ZrB_2, HfB_2 and TiB_2. *Acta Mater* 2007, **55**: 5999–6010.
[24] Zapata-Solvas E, Jayaseelan DD, Brown PM, *et al*. Effect of La_2O_3 addition on long-term oxidation kinetics of ZrB_2-SiC and HfB_2-SiC ultra-high temperature ceramics. *J Eur Ceram Soc* 2014, **34**: 3535–3548.
[25] Nickel KG. *Corrosion of Advanced Ceramics: Measurement and Modelling*. Dordrecht, the Netherlands: Kluwer Academic Publishers, 1994.
[26] Harrison RW, Lee WE. Mechanism and kinetics of oxidation of ZrN ceramics. *J Am Ceram Soc* 2015, **98**: 2205–2213.
[27] Deal BE, Grove AS. General relationship for the thermal oxidation of silicon. *J Appl Phys* 1965, **36**: 3770–3778.